CrossMark

RESEARCH ARTICLE

Vortex dynamics and wall shear stress behaviour associated with an elliptic jet impinging upon a flat plate

J. Long[1] · T. H. New[1]

Abstract Vortical structures and dynamics of a $Re_h = 2100$ elliptic jet impinging upon a flat plate were studied at $H/d_h = 1$, 2 and 4 jet-to-plate separation distances. Flow investigations were conducted along both its major and minor planes using laser-induced fluorescence and digital particle image velocimetry techniques. Results show that the impingement process along the major plane largely consists of primary jet ring-vortex and wall-separated secondary vortex formations, where they subsequently separate from the flat plate at smaller $H/d_h = 1$ and 2 separation distances. Key vortex formation locations occur closer to the impingement point as the separation distance increases. Interestingly, braid vortices and rib structures begin to take part in the impingement process at $H/d_h = 4$ and wave instabilities dominate the flow field. In contrast, significantly more coherent primary and secondary vortices with physically larger vortex core sizes and higher vortex strengths are observed along the minor plane, with no signs of braid vortices and rib structures. Lastly, influences of these different flow dynamics on the major and minor plane instantaneous and mean skin friction coefficient levels are investigated to shed light on the effects of separation distance on the wall shear stress distributions.

✉ T. H. New
dthnew@ntu.edu.sg

[1] School of Mechanical and Aerospace Engineering, Nanyang Technological University, 50 Nanyang Avenue, Singapore 639798, Singapore

1 Introduction

Impinging jets have seen extensive engineering applications as an effective technique for heating, cooling or drying purposes. Typical applications include drying of paper and textiles, as well as cooling of gas turbine blades and microelectronic components, among others. It should not come as a surprise that extensive prior investigations have been carried out by researchers working in the areas of heat transfer characteristics and flow dynamics. Some earlier studies would include Martin (1977), Goldstein et al. (1990), Lee et al. (1994), Cornaro et al. (2001), Lim et al. (2007) and Koseoglu and Baskaya (2008). In particular, Koseoglu and Baskaya (2008) showed that local heat transfer rates are linked to the turbulence levels in the jet and radial flow acceleration along the impingement plate for both circular and elliptic jets. The majority of past investigations focused upon the impingement behaviour associated with the classical circular jet and mainly dealt with the effects of Reynolds number, jet-to-surface separation distance, impingement surface geometry and others.

One of the earliest quantitative studies on impinging jets through the use of digital particle image velocimetry (DPIV) technique was performed by Landreth and Adrian (1990) to measure the velocity field of a circular jet impingement scenario at a low Reynolds number. Velocity profiles of the resulting flow field and vorticity maps indicate that surface boundary layer separation occurs and leads to the subsequent formation of secondary vortices. On the basis of this quantitative investigation, more information on circular jet impingement such as vortex dynamics, wall shear stress distribution and dynamic velocity fields were further obtained through various experimental techniques such as laser-induced fluorescein (LIF), DPIV, laser Doppler velocimetry (LDV), et cetera. Some of these

investigations would include those reported by Cornaro et al. (1999), Phares et al. (2000), Fleischer et al. (2001), Fairweather and Hargrave (2002), Esirgemez et al. (2007), EI Hassan et al. (2012) and New and Long (2015), among many others. Heat transfer characteristics have also been comprehensively summarized by Jambunathan et al. (1992), though they are beyond the scope of the present work. As a result, the flow and heat transfer characteristics associated with a circular jet impinging upon solid boundaries are at present relatively well-understood.

It is well known that a circular jet produces axisymmetric vortical structures along the shear layers, but the vortical behaviour of an elliptic jet is far more complex because of its non-constant diameter along its circumference. Gutmark and Ho (1986) conducted flow visualizations to demonstrate the presence of axis-switching phenomenon, and Ho and Gutmark (1987) determined that the overall entrainment ratio of an aspect-ratio AR = 2 elliptic jet was much greater than that of a comparable circular jet. They also confirmed that the non-uniform distribution of the jet momentum thickness around the elliptic jet circumference underpins the axis-switching phenomenon. Hussain and Husain (1989) and Husain and Hussain (1991, 1993) conducted an extensive series of experiments to show that the vortical structures of an elliptic jet undergo complex three-dimensional deformations, which in turn lead to various unique entrainment and other turbulent phenomenon. Rib structures were found and their formations and interactions with the vortex roll ups were explained in great detail.

Looking at the preceding studies, it is surprising that little information on the fundamental flow dynamics associated with elliptic jet impingements is available. Instead, most of the reported studies surrounding impinging elliptic jets emphasized upon their heat transfer characteristics. For instance, Lee et al. (1994) reported upon the heat transfer characteristics for AR = 2.14 elliptic impinging jets. They found that the Nusselt number for the elliptic jet in the impingement region was higher than that for a circular jet. They also discovered the existence of second and third maxima in local Nusselt number distributions at a separation distance of $H/d_h = 2$ for $Re_h = 10,000$ and 20,000 elliptic jets (i.e. where H is the separation distance, d_h is the jet hydraulic diameter and Re_h is the jet Reynolds number based on d_h), and attributed this phenomenon to the wall-separated secondary vortices. Lee and Lee (2000) investigated the effects of elliptic jet aspect ratio on stagnation region heat transfer performance and summarized the correlation of stagnation point Nusselt number with parameters such as separation distance and jet aspect ratio. More complicated elliptic jet arrays impinging upon a flat plate and their resulting behaviour as the aspect ratio and Reynolds number were varied, were also investigated by Yan et al. (2004), Yan and Mei (2006) and Caliskan et al. (2014).

One of the few studies that offered some insights into impinging elliptic jet vortical structures and behaviour was reported by Lee and Lee (2000), where they conducted flow visualizations on a $Re_h = 10,000$, AR = 2 elliptic impinging jet at a fixed separation distance of $H/d_h = 2$. They observed the presence of axis-switching phenomenon even when the impingement plate was present, where the vortical structures are different along the major-and minor planes due to the azimuthal curvature variation associated with the elliptic jet. However, no attempts to look into the effects of separation distance were made. A study on the flow field of confined elliptic jet impingements was investigated by Koseoglu and Baskaya (2008) through mean velocity and turbulence measurements using laser Doppler anemometry (LDA). The experiments were conducted with a $Re_h = 10,000$ elliptic jet at separation distances of $H/d_h = 2$–6. They presented mean radial and axial velocity, as well as turbulence intensity results, and observed much higher spreading rates for the elliptic jet along the minor plane. However, the above studies were limited to only flow visualization snapshots, mean flow and turbulence statistics, which yield little information on the overall elliptic jet impingement flow dynamics.

To address the lack of detailed knowledge on the flow structures and behaviour surrounding elliptic jet impingements, the present study aims to understand the effects of jet-to-plate separation distance on the vortical structures and behaviour of an AR = 3 elliptic jet impinging upon a flat plate and to provide more concrete flow dynamics information through LIF and DPIV techniques. A $Re_h = 2100$ elliptic jet at jet-to-plate separation distances of $H/d_h = 1$, 2 and 4 was investigated. All coherent vortical structures including elliptic jet ring-vortices, structures arising from axis-switching behaviour and wall-separated vortices will be tracked from their initiations to their eventual breakup along the flat plate. Instantaneous and mean skin friction coefficient distributions will also be determined to understand the effects of jet-to-plate separation distance upon the wall shear stress levels, as well as to correlate dynamic vortical events with the resulting skin friction coefficient distributions.

2 Experimental apparatus and procedures

2.1 Jet impingement apparatus

The present study was carried out using a recirculating water tank facility with appropriately designed jet apparatus that was relatively similar to those used successfully by the authors for different jet-based studies (New and Tsovolos 2009, 2011, 2012; New and Tsioli 2011; Long and New 2015). The flow circuit began from a centrifugal

pump which channelled water from a small reservoir and delivered them into the test nozzle, before exhausting into the water tank with internal dimensions of 800 mm $(L) \times 400$ mm $(W) \times 400$ mm (H). Water level in the water tank was maintained constant throughout the entire study by diverting water overflow back into the small reservoir from two PVC pipes located at the end wall of the water tank, thus completing the flow circuit. An electromagnetic flow meter and a needle valve were employed to monitor and maintain the flow rate at a fixed value, respectively. Upstream of the jet exit, the water was conditioned by a jet apparatus that consisted of a diffuser, honeycomb straighteners, three layers of fine screens and a 25:1 circular-to-elliptic contraction chamber.

The Reynolds number of the elliptic jet based on its hydraulic diameter was maintained at $Re_h = Ud_h/\upsilon \approx 2100$, where U is the mean jet exit velocity and υ is the kinematic viscosity of the water at experimental conditions. The major and minor diameters of the elliptic jet measured 36.7 and 12.3 mm, respectively (i.e. AR = 3), which gave rise to an estimated hydraulic diameter of approximately $d_h = 17.4$ mm. Figure 1 shows the mean streamwise velocity and turbulence intensity profiles at approximately $x/d_h = 0.2$ downstream of the jet exit along both major and minor planes, as determined from mean DPIV measurements taken for the elliptic jet under freely exhausting conditions. Under such conditions, any jet shear layer instabilities and subsequent vortex roll-up formations were due to the inherent hydrodynamic wave instabilities, and no obstacle was blocking the elliptic jet flow in any way with the water tank sufficiently long so as not to affect the natural shear layer instabilities in any significant manner.
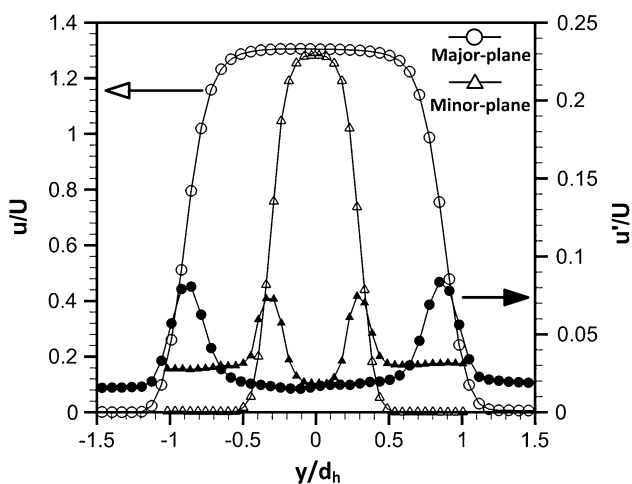

Fig. 1 Mean streamwise velocity and turbulence intensity profiles for the freely exhausting $Re_h = 2100$ elliptic jet at $x/d_h = 0.2$ downstream of the jet exit

Note that the present study focused on naturally occurring jet impingement behaviour, where no flow forcing was used on the elliptic jet to accentuate the vortex roll-up formations and the effects of any jet perturbation amplitude or frequency (Longmire and Duong 1996; New and Tsovolos 2009) were not pursued here. The impingement target was manufactured from a Plexiglas flat plate, which was entirely covered with thin black adhesive paper in order to avoid significant light reflections caused by laser sheet illuminations during the LIF and DPIV experiments. The thickness of the self-adhesive paper was only 0.09 mm, which introduced negligible influences on the jet-to-plate separation distance. The dimensionless separation distances from the jet exit to the impingement flat plate used in the present investigation were $H/d_h = 1$, 2 and 4.

2.2 LIF and DPIV techniques

LIF technique was used here to better understand the vortex structures and behaviour qualitatively. This technique has been used to obtain informative jet flow structural and behavioural details under different jet flow scenarios successfully by New and Tay (2006), Lim et al. (2006) and New and Tsovolos (2012). Fluorescein disodium fluorescent salt was dissolved into and premixed with the jet fluid uniformly prior to the latter exhausting into the water tank, where the fluorescent dye was illuminated by a thin laser sheet from one side of the water tank aligned with the jet centreline. The laser sheet was produced by a 1 W, 532 nm wavelength, LaVision continuous-wave diode-pumped solid state (DPSS) laser and sheet-forming optics [i.e. similar to procedures adopted by Shi et al. (2013)]. A remotely controlled Canon digital single-lens reflex (DSLR) camera with a 50 mm, f1.4 lens mounted above the water tank was used to record the LIF visualizations. The videos were recorded in 1920 px × 1080 px resolution at 25 frames per second, from which still flow images were then extracted on a workstation for subsequent analysis.

Figure 2 shows the experimental set-up used to measure 2D velocity fields for the present impinging elliptic jets, based on a Dantec Dynamics 2D DPIV system. Despite the 3D nature of the resulting flow field, lower-order 2D flow measurement technique (as compared to higher-order 3D tomographic DPIV measurement technique) remains satisfactory in terms of obtaining accurate measurement of the velocity fields, provided that multiple measurements planes are used, as demonstrated by New and Tsovolos (2009) and New and Tsai (2007). The illumination source was a Quantel Evergreen 200 mJ/pulse double-pulsed Nd:YAG laser system with a laser sheet thickness of approximately 2 mm. The laser beams were expanded into thin laser sheets through sheet-forming optics at a height that coincided with the jet centerline. The time interval between

Fig. 2 Experimental schematics of the DPIV measurement set-up
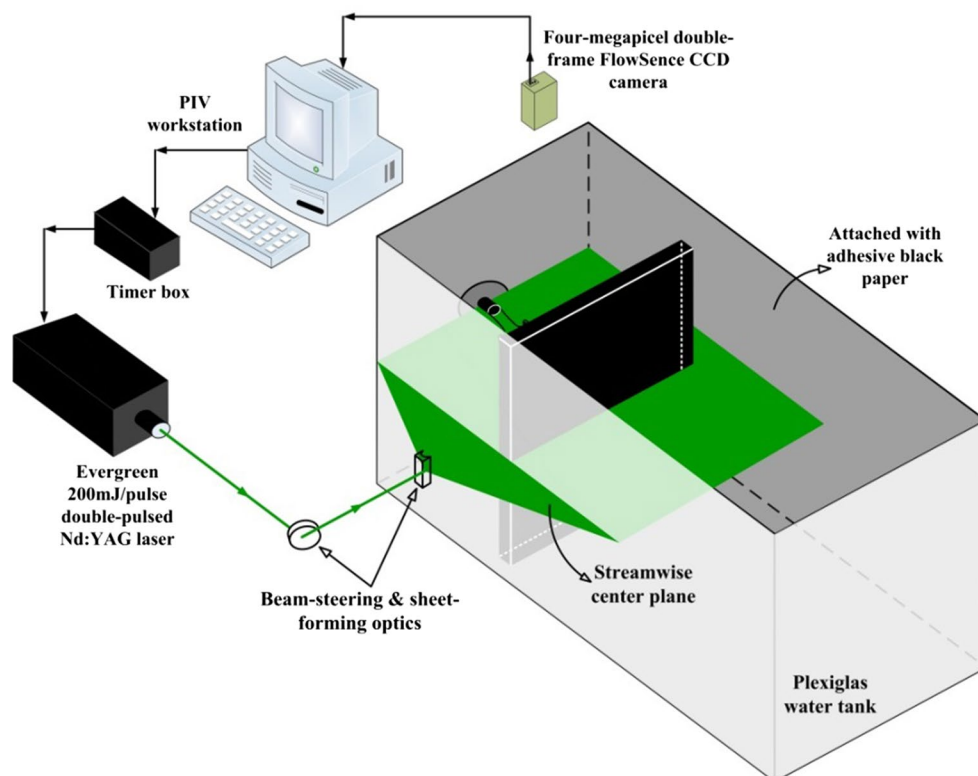
the two laser pulses was kept at 3 ms throughout the study. Twenty-micrometer-sized, 1.03 g/cm^3 polyamide seeding particles were used as tracers for the DPIV experiments and premixed with the water in the reservoir and water tank uniformly prior to the measurements.

Image pairs of the illuminated particles were captured using a four-megapixel double-frame FlowSense CCD camera mounted above the water tank and facing the laser sheet plane perpendicularly. In order to track the dynamics of the impinging elliptic jets well, the CCD camera was subjected to a 2 × 1 CCD binning, which allowed capturing of the particle image pairs at 14 Hz, but at a reduced resolution from 2048 px × 2048 px to 2048 px × 1024 px. While this acquisition rate was slightly lower than those used by New and Tsovolos (2009, 2011, 2012) and New and Tsioli (2011) in their jet flow studies earlier, it remained sufficiently fast to track the vortex structures and their flow dynamics, as will be seen in the results presented later. On the other hand, the higher 2:1 aspect-ratio effective CCD camera resolution (i.e. 2048 px × 1024 px) here allowed better framing of the impinging elliptic jet flows within the regions of interest under most experimental conditions than a 4:3 aspect-ratio CCD camera resolution (i.e. 1600 px × 1200 px) used in the above-mentioned earlier studies. This was especially the case when capturing the vortex structures and their flow developments along the flat surface was one of the objectives here, where the vortex structures tended to convect and develop over
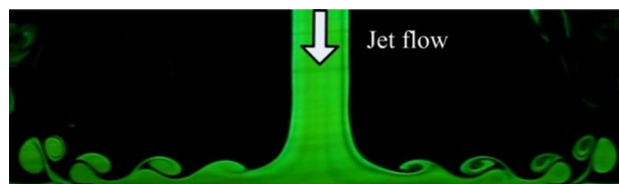

Fig. 3 Example of a typical symmetrical flow field obtained along the elliptic jet minor plane at $H/d_h = 2$ using LIF technique

significant distances. As Fig. 3 shows that the LIF-visualized flow fields were highly symmetric about the impingement axis, DPIV measurements were conducted for half of the impinging jet flow fields to improve DPIV measurement resolution. A total number of 500 image pairs were acquired for each test case, where it has been shown to provide satisfactory convergence for mean results evaluation.

The captured image pairs were analysed by Dantec DynamicStudio™ software using a two-step multigrid cross-correlation scheme. An initial interrogation window size of 128 px × 128 px and a final interrogation window size of 32 px × 32 px were used with 50 % overlaps in both horizontal and vertical directions. The sub-pixel accuracy was approximately 0.1 pixel based on the cross-correlation procedures. The resultant raw velocity field vectors were then validated using global validation schemes (i.e. peak, range and moving-average validations) to eliminate any spurious vectors. Thereafter, the validated velocity field

vectors were subjected to a 3-point by 3-point neighbour scheme to yield the final vector maps and other associated flow quantities such as vorticity, λ_2-criterion and wall shear stress. More information on the overall DPIV experimental uncertainties has been elaborated by New and Long (2015) previously, and readers are encouraged to refer to that. The skin friction coefficient was also calculated based on similar procedures adopted by New and Long (2015) and Long and New (2015), and readers are advised to refer to those papers for more procedural details. Moreover, the uncertainty level associated with skin friction coefficient (as based on its standard definition) have been estimated to be within ±4.6 %, according to the procedures outlined by Moffat (1988), Coleman and Steele (1995) and New and Long (2015). This uncertainty level remains adequate for the purpose of the present study, as it had been for New and Long (2015).

The λ_2-criterion, as proposed by Jeong and Hussain (1995) previously, was used here to detect the vortex cores more reliably from the DPIV velocity results during the jet impingement process. It should be mentioned that it has been used by EI Hassan et al. (2012) and New and Long (2015) on impinging jets successfully in earlier studies. Specifically, pressure tends to have a local minimum in a vortex on the axis of a circulatory or swirling motion. If one takes the gradient of the Navier–Stokes equation, it can be shown that

$$a_{i,j} = -\frac{1}{\rho}p_{,ij} + \nu u_{i,jkk}, \qquad (1)$$

where $a_{i,j}$ is the acceleration gradient, while $p_{,ij}$ is the Hessian of pressure and symmetric. Subsequently, $a_{i,j}$ can be decomposed into symmetric and antisymmetric components as

$$a_{i,j} = \left[\frac{DS_{ij}}{Dt} + \Omega_{ik}\Omega_{kj} + S_{ik}S_{kj}\right] + \left[\frac{D\Omega_{ij}}{Dt} + \Omega_{ik}S_{kj} + S_{ik}\Omega_{kj}\right]. \quad (2)$$

The symmetric part of Eq. (2) is

$$\frac{DS_{ij}}{Dt} - \nu S_{ij,kk} + \Omega_{ik}\Omega_{kj} + S_{ik}S_{kj} = -\frac{1}{\rho}p_{,ij} \qquad (3)$$

The first two terms on the left-hand side of Eq. (3) represent the unsteady irrotational straining and viscous effects. To discard these two effects, these two terms will not be considered. Two eigenvalues of the tensor $p_{,ij}$ are required to ensure the occurrence of a pressure minimum due to vortical motion. Thus, a vortex core is defined as a connected region with two negative eigenvalues of $S^2 + \Omega^2$. $S^2 + \Omega^2$ only has real eigenvalues since it is symmetric. If λ_1, λ_2, λ_3 are assumed to be the eigenvalues and $\lambda_1 \geq \lambda_2 \geq \lambda_3$, a vortex core is deemed to have been identified if $\lambda_2 < 0$. All λ_2-criterion results determined within the present study were obtained through Dantec DynamicStudio™ software

which has the necessary tools incorporated to calculate λ_2-criterion during the post-processing stage.

3 Results and discussions

Typical visualization snapshots along both the major and minor planes for the freely exhausting elliptic jet flow are presented in Fig. 4. The results show that different vortical structures are produced along the major and minor planes, where the rolling-up of the shear layer along the minor plane initiates at approximately $x/d_h = 1.7$ from the jet exit, which is earlier than that along the major plane at approximately $x/d_h = 2.4$. Significant differences in the physical sizes of the vortex roll-ups along the two planes can also be seen by the comparison here. According to Hussain and Husain (1989), Fig. 4 indicates that the momentum thickness along the minor plane is much thinner than that along the major plane, which in turn produces earlier and larger vortex roll-ups with higher vortex strengths. Along the minor plane, the ring-vortices grow in size gradually and vortex engulfment between adjacent ring-vortices occurs as they convect further downstream. In contrast, braid vortices and rib structures are produced along the major plane, where the latter are produced as a result of interactions between the elliptic jet vortex roll-ups and braid vortices before $H/d_h = 4$.

Correlating the flow images in Fig. 4, it is clear that the vortex roll-ups undergo axis-switching behaviour and similar observations have been made by Ho and Gutmark (1987), Quinn (1989), Hussain and Husain (1989) and New and Tsovolos (2011). Observations from Fig. 4 indicate that elliptic jet impingement behaviour will be highly sensitive towards the separation distance, since the states of the elliptic jet vortical structures vary significantly as they convect away from the jet exit, as compared to circular jet impingement. To further verify the presence of axis-switching behaviour in the present elliptic jet under freely exhausting conditions, mean half-jet widths along the major and minor planes were determined from mean DPIV measurement results and presented in Fig. 5. It can be observed that a crossover point is located at approximately $x/d_h = 5.8$ and thus demonstrates the existence of axis-switching behaviour. This location is also in good agreement with New and Tsovolos (2011) where their AR = 3 elliptic jet under relatively similar flow conditions show a crossover point at $x/d_h = 5.7$.

Figure 6 shows time-sequenced LIF flow visualization images associated with the impinging elliptic jet at a separation distance of $H/d_h = 4$ as taken along its major plane. Flow developments of all key vortical structures from their initiations to breakup are tracked, including the jet ring-vortex (i.e. A), wall-separated vortex (i.e. S_1), rib

Fig. 4 LIF flow visualization snapshots for the present $Re_h = 2100$ elliptic jet along both its major and minor planes under freely exhausting conditions
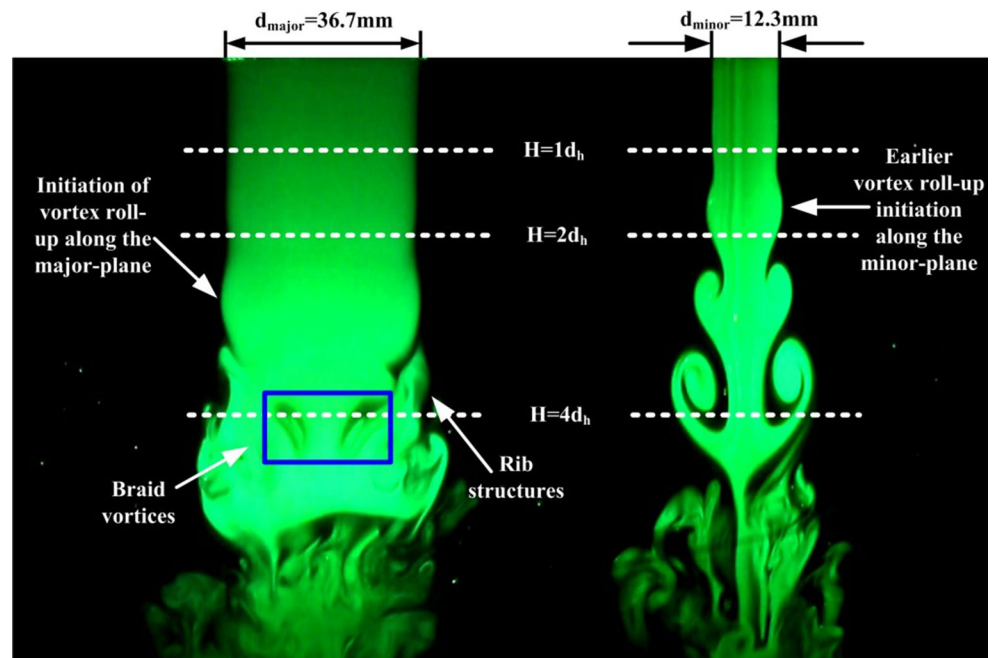
structure (i.e. R) and braid vortex. In order to describe the rather significant vortical changes during the impingement process, nomenclatures such as ring-vortex initiation, wall-separated vortex initiation, vortex-dipole formation and vortex separation, similar to those used by the authors in their earlier studies will be used here as a matter of consistency. For instance, ring-vortex initiation refers to where the jet ring-vortex first initiates along the jet shear layer. It should be mentioned that the wall boundary layer separates from the impingement surface in the presence of an adverse pressure gradient. While all necessary care had been taken during the course of the study, flow behaviour could still have been influenced by the confined experimental environment associated with a finite-size water tank, however minute the influences might have been.

Moreover, the locations for wall boundary layer separation may not always be accurately captured by flow visualizations or DPIV measurement, due to the discontinuous nature of these techniques. However, since wall-separated secondary vortices are formed as a result of wall boundary layer separations, the positions of secondary vortices can be used reliably as indications of wall boundary layer separation locations. In the present study, the initiation locations of the secondary vortices refer to where they are first clearly discerned from the instantaneous flow visualizations and DPIV results. Vortex-dipole formation denotes where wall-separated secondary vortices merge with the opposite-signed primary ring-vortices to form mushroom-shaped vortex structures. Finally, vortex separation is where a vortex-dipole detaches from the flat plate. Six flow instances are presented in the figure to demonstrate a sequence of
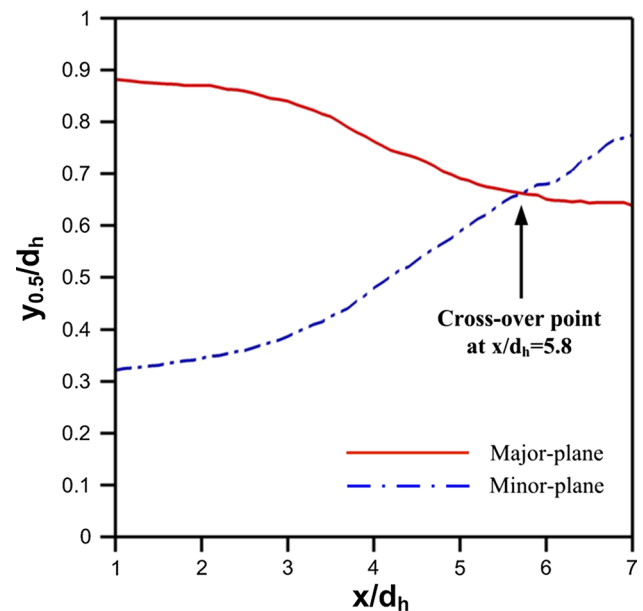

Fig. 5 Mean half-jet width profile for the present $Re_h = 2100$ elliptic jet along the major and minor planes under freely exhausting conditions

the unique jet impingement vortex structures and how they subsequently behave and interact. In this case, the first flow visualization image is set arbitrarily to $t = 0$ s and shows the jet ring-vortex initiation, while the subsequent key flow behaviour and vortical structures will be showcased in the next five instances.

According to Fig. 6, the initiation of a jet ring-vortex (i.e. A) occurs at about the same downstream location as

Fig. 6 Time-sequenced major plane LIF flow images depicting the vortical behaviour associated with elliptic jet-flat plate impingement at $H/d_h = 4$ separation distance. **a** $t = 0$ s, **b** $t = 0.20$ s, **c** $t = 0.36$ s, **d** $t = 0.44$ s, **e** $t = 0.56$ s, **f** $t = 0.72$ s
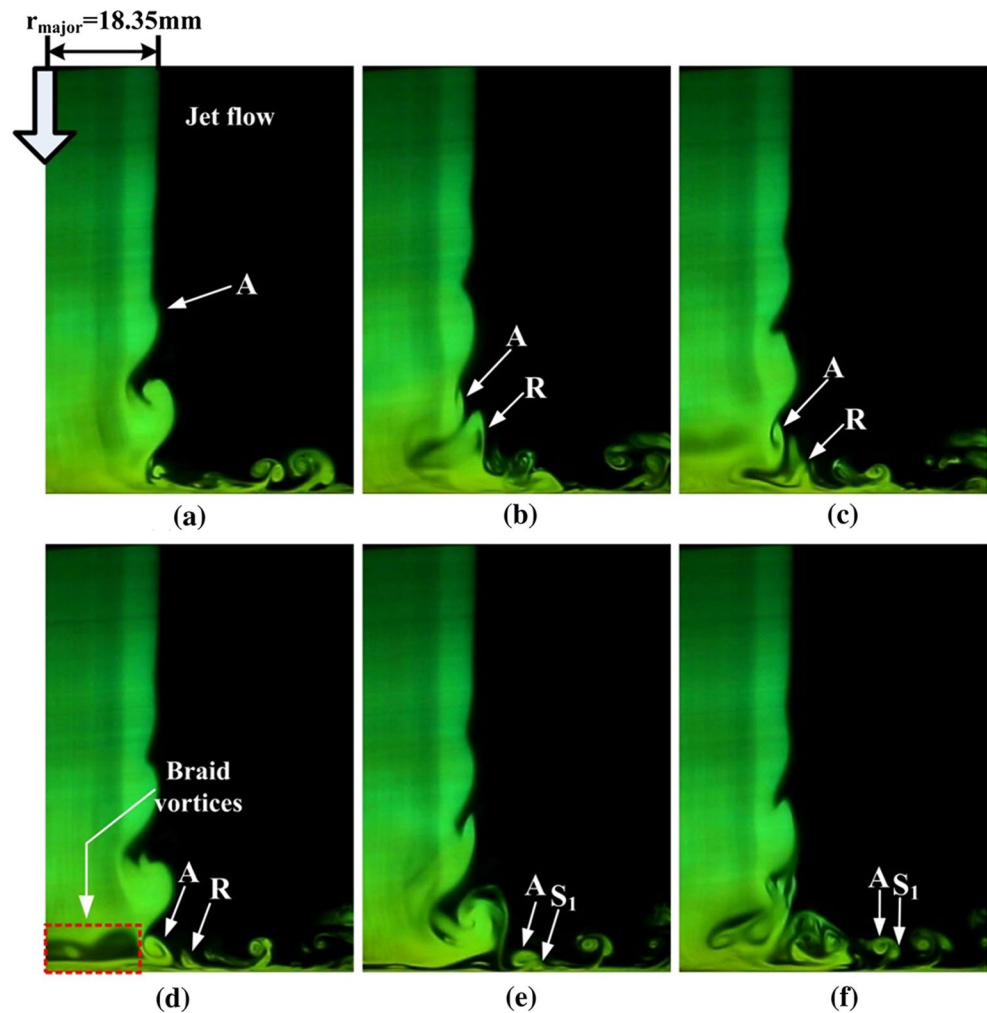

with the free elliptic jet shown in Fig. 4 previously. Along the major plane, the jet ring-vortex is seen as moving laterally inwards and towards the jet centerline by the time it impinges upon the flat plate. A rib structure is observed to form adjacent to the jet ring-vortex prior to impingement as well and depicted in Fig. 6b. Both the jet ring-vortex and rib structure move radially away from the impingement point after they impinge upon the flat plate and convect along the flat plate, as shown in Fig. 6d–f. The rib structure subsequently breaks down rapidly, though the jet ring-vortex continues to lead to wall boundary layer separation that produces a secondary vortex (i.e. S_1). Further downstream, they combine to produce a mushroom-shaped vortex-dipole which detaches from the flat plate, as shown in Fig. 6e, f. Interestingly, braid vortices can also be observed to form just above the flat plate at this separation distance, but they disappear rapidly after they impinge upon the flat plate, as can be seen in Fig. 6d, e.

Figure 7 shows the time-sequenced instantaneous DPIV velocity fields and λ_2-criterion-filtered regions corresponding to the typical major plane flow behaviour observed in

Fig. 6 (i.e. $H/d_h = 4$), as well as the corresponding instantaneous skin friction coefficient distributions. In this study, a minimum λ_2 cut-off value of -400 and a maximum λ_2 cut-off value of -10 are used here to better isolate the vortex core regions from the background values. Furthermore, corresponding instantaneous skin friction coefficient distributions are presented above each instantaneous DPIV velocity result to ease direct comparisons and analysis, which will allow better correlations between the vortex structures and how their behaviour affects the instantaneous wall shear stress distribution.

Similar to Fig. 6, the first DPIV measurement result is arbitrarily set to $t = 0$ s and represents the first instance when jet ring-vortex is initiated along the jet shear layer. Note that there is a slight time discrepancy between selected instantaneous LIF visualization results and DPIV results since different measurement frequencies were used for LIF visualization (i.e. 25 Hz) and DPIV (i.e. 14 Hz) measurements. Nevertheless, the maximum time discrepancy is 0.02 s, which is sufficiently small for the present comparison purposes. Comparing Figs. 6 and 7, it can be

Fig. 7 Instantaneous major plane DPIV velocity fields and λ_2-criterion-*highlighted* regions with corresponding instantaneous skin friction coefficient associated with the present elliptic jet-flat plate impingement at $H/d_h = 4$ separation distance. **a** $t = 0$ s, **b** $t = 0.21$ s, **c** $t = 0.36$ s, **d** $t = 0.43$ s, **e** $t = 0.57$ s, **f** $t = 0.71$ s
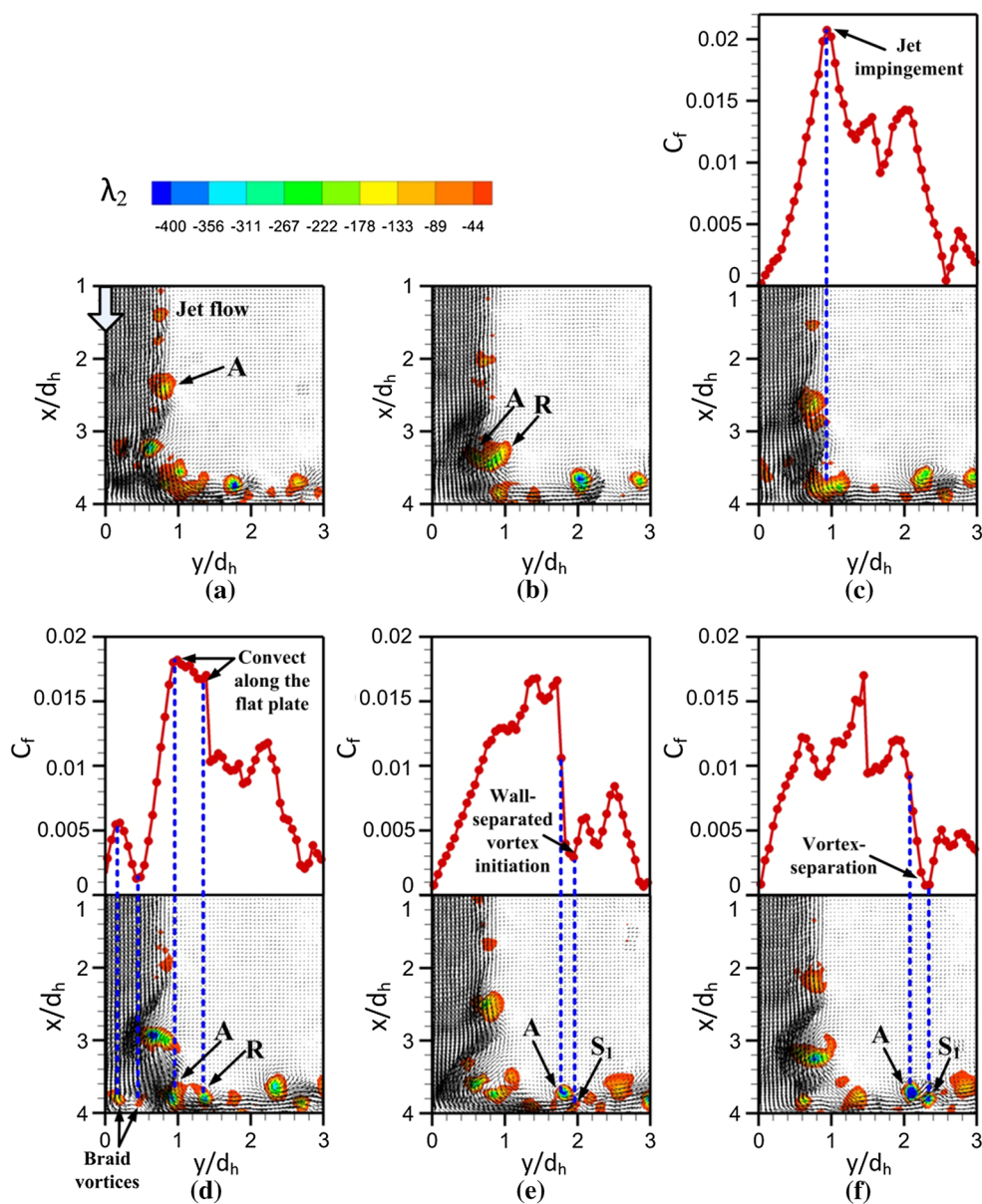
seen that the flow developments of jet ring-vortex (A), wall-separated vortex (S_1), rib structure (R) and braid vortices are all consistent with the qualitative flow visualizations. However, with the availability of these DPIV results, the locations of the key vortical behaviours for the impinging elliptic jet can now be extracted and quantified with better accuracy. In particular, the results show that the jet ring-vortex initiates at approximately $x/d_h = 2.4$, while rib structure and braid vortices occur just upstream of the flat plate, which are in good agreement with the freely exhausting elliptic jet discussed earlier. This indicates that the presence of the flat plate does not produce significant adverse pressure gradient that might have affected vortical behaviour significantly prior to the jet impingement. Wall-separated vortex initiation and vortex separation locations can also

be determined from Fig. 7e, f, which are estimated to be approximately $y/d_h = 1.9$ and 2.2, respectively.

Corresponding instantaneous skin friction coefficients are included in Fig. 7 to look at their variations associated with the various key vortex structures and behaviour. Note that while flow separations could in theory be identified by zero instantaneous local skin friction coefficient values, the moderate 14 Hz DPIV acquisition rate was unlikely to have captured the exact moments when the wall boundary layer separated from the flat plate. Hence, it will be more appropriate to identify sudden reductions in the skin friction coefficient levels as indications of wall boundary layer separation events. Note that there are a few distinctive peaks in the instantaneous skin friction coefficient distributions, which correspond to the impingement and
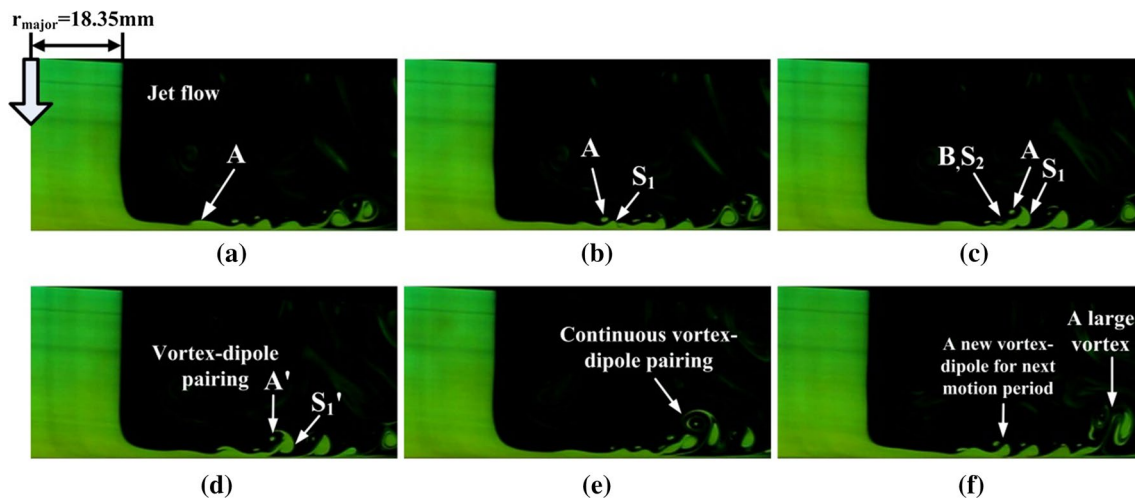
Fig. 8 Time-sequenced major plane LIF flow images depicting the vortical behaviour associated with elliptic jet-flat plate impingement at $H/d_h = 2$ separation distance. **a** $t = 0$ s, **b** $t = 0.16$ s, **c** $t = 0.44$ s, **d** $t = 0.52$ s, **e** $t = 1.08$ s, **f** $t = 1.52$ s

convection of the vortex structures along the flat plate. For instance, Fig. 7c shows that the jet ring-vortex and rib structure produce the highest skin friction coefficient peak at approximately $C_f = 0.021$ when they impinge upon the flat plate. A moment later, Fig. 7d shows that braid vortices impinging on the flat plate within the jet core lead to a small sudden increase in the local skin friction coefficient close to the impingement point, with a peak value of approximately $C_f = 0.006$ at $y/d_h = 0.2$. The peak associated with this phenomenon does not appear in subsequent plots of Fig. 7.

As the jet ring-vortex and rib structure convect along the flat plate, they produce two closely spaced local peaks in the skin friction coefficient distribution, as highlighted in Fig. 7d. These two peak values remain relatively high at approximately $C_f = 0.018$ and 0.017, respectively, until the rib structure breaks up with the jet ring-vortex producing a lower skin friction coefficient value of approximately $C_f = 0.01$, as shown in Fig. 7e. At the same time, an opposite-signed secondary vortex occurs due to wall boundary layer separation, which leads to a drastic reduction of the skin friction coefficient level to a local minimum value of $C_f = 0.003$. Subsequently, separation of the vortex-dipole from the flat plate reduces the skin friction coefficient further, as can be seen from Fig. 7f. All in all, the impingements of jet ring-vortex and rib structure upon the flat plate produce distinct peaks in the skin friction coefficient distributions, before the peak values decrease as the jet deflects gradually and the rib structure breaks up rapidly. The appearance of a wall-separated secondary vortex and vortex separation lead to further dramatic reductions in the skin friction coefficient to extremely low levels.

When the separation distance is reduced to $H/d_h = 1$ and 2, large-scale ring-vortices are not observed along the jet shear layers along the major plane, not to mention rib structures and braid vortices. These are the most significant flow differences as compared to $H/d_h = 4$ test case. As shown in Figs. 8 and 9, the key vortical flow behaviour for $H/d_h = 2$ test case along the major plane only consists of jet ring-vortices and wall-separated vortices that are physically much smaller than those observed for the $H/d_h = 4$ test case. These changes due to a reduction in the separation distance are similar to those observed for circular jet-flat plate impingements by Long and New (2015) previously. However, the use of an elliptic jet here leads to physically smaller vortical structures.

Due to the much smaller separation distance, the jet ring-vortex (i.e. A) is now initiated along the flat plate after impingement instead of along the jet shear layer in the major plane. The jet ring-vortex initiation location is approximately $y/d_h = 1.9$, as shown by the DPIV results presented in Fig. 9a. A wall-separated vortex (i.e. S_1) is formed subsequently, but further away from the impingement point as compared to the $H/d_h = 4$ test case. As a result, vortex separation occurs correspondingly further downstream, estimated to be at approximately $y/d_h = 2.3$ and 2.7, as depicted in Fig. 9b, c respectively. Intriguingly, pairing between the vortex-dipole (i.e. A and S_1) with its upstream neighbour (i.e. B and S_2) to form a new vortex-dipole (i.e. A' and S_1') occurs after vortex separation, instead of them convecting along the flat plate independently like what was observed for the $H/d_h = 4$ test case previously. This pairing process continues and typically involves about three to four vortex-dipoles, which leads to a relatively larger vortex entity that travels to approximately $y/d_h = 3.6$. At that point in time, a new vortex-dipole will begin to form at $y/d_h = 2.1$, which typically means that the multiple pairing process will repeat again. This shows that

Fig. 9 Instantaneous major plane DPIV velocity fields and λ_2-criterion-*highlighted* regions with corresponding instantaneous skin friction coefficient associated with elliptic jet-flat plate impingement at $H/d_h = 2$ separation distance. **a** $t = 0$ s, **b** $t = 0.14$ s, **c** $t = 0.43$ s, **d** $t = 0.50$ s, **e** $t = 1.07$ s, **f** $t = 1.50$ s
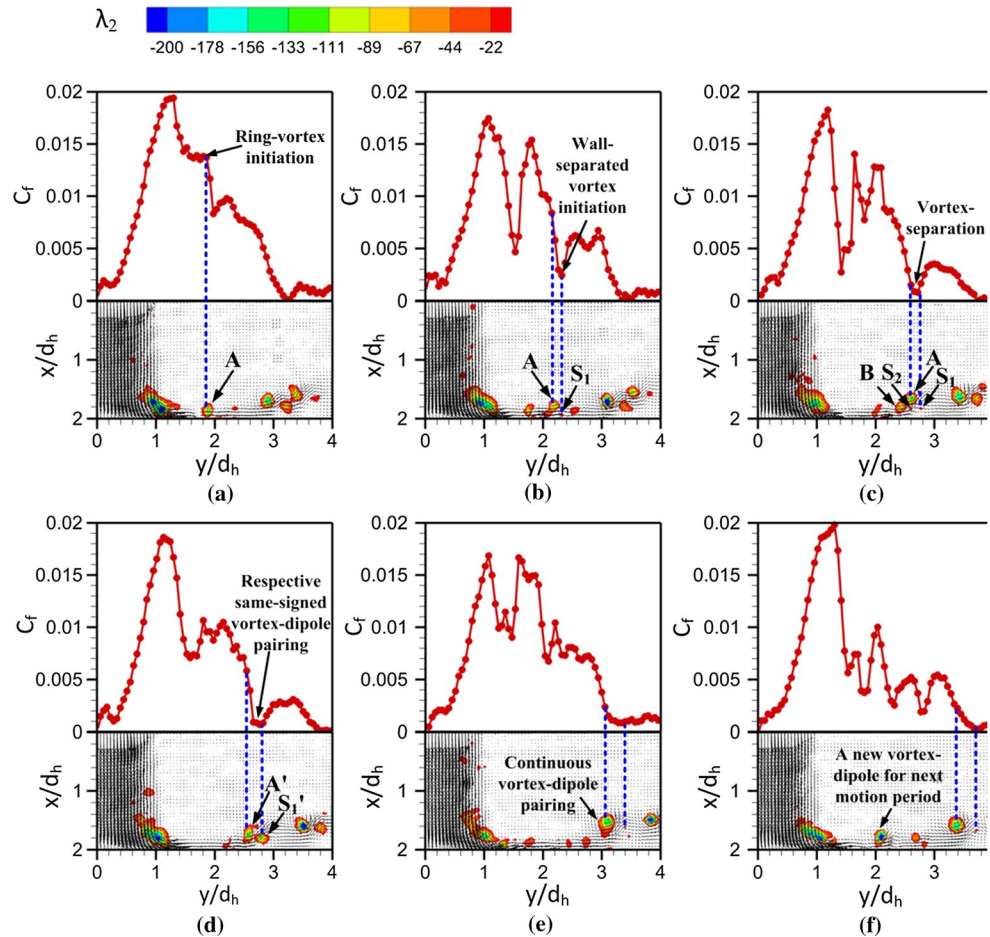
the intriguing vortical amalgamation behaviour is actually periodic, as shown in Figs. 8f and 9f. In comparison, circular jet-flat plate impingement at relatively similar separation distance and flow conditions does not produce this periodic vortical amalgamation behaviour. Instead, the vortex-dipoles convect along the flat plate independently with relatively larger vortex-dipole sizes.

As for the instantaneous skin friction coefficient distribution for the $H/d_h = 2$ test case, it increases rapidly from close to zero near the impingement point to register the first and highest peak at approximately $y/d_h = 1.2$ with a value of approximately $C_f = 0.02$. However, this highest peak is not associated with any distinct vortical structures, which is in direct contrast to the $H/d_h = 4$ test case where the first and highest peak value is linked to the impinging jet ring-vortex and rib structure. While the λ_2-criterion results show a highlighted region from $y/d_h = 0.8$ to 1.2, this is unlikely to be associated with a vortex core. Instead, this is likely due to the abrupt change in the jet flow direction immediately after it impinges upon the flat plate, which in turn leads to large velocity gradients. The initiation of the jet ring-vortex after impingement ensures that the corresponding instantaneous skin friction coefficient still maintains

at a relatively high value of approximately $C_f = 0.014$, as depicted in Fig. 9a. The effects of subsequent initiation of the wall-separated vortex on the skin friction coefficient remain consistent with earlier discussions for the $H/d_h = 4$ test case, which brings about a significant decrease in its level. Further reductions occur due to vortex separation behaviour, before the first vortex-dipole pairing leads to a slight increase in skin friction coefficient.

Finally, Fig. 10 shows the corresponding experimental results for the $H/d_h = 1$ test case. As the flow behaviour is significantly more muted than those observed at larger separation distances, only one representative set of results is presented here. Similar to the $H/d_h = 2$ test case, no jet ring-vortex is produced prior to jet impingement. However, the most interesting difference here is that there are no clear observations of primary jet ring-vortices and wall-separated secondary vortices along the impingement surface as well. Instead, only a few wave instabilities are produced close to the flat plate, where they initiate at approximately $y/d_h = 1.8$. These wave instabilities subsequently travel along and separate from the flat plate, which then finally coalesce together to produce a large vortex entity located at approximately $y/d_h = 3.6$. The vortex
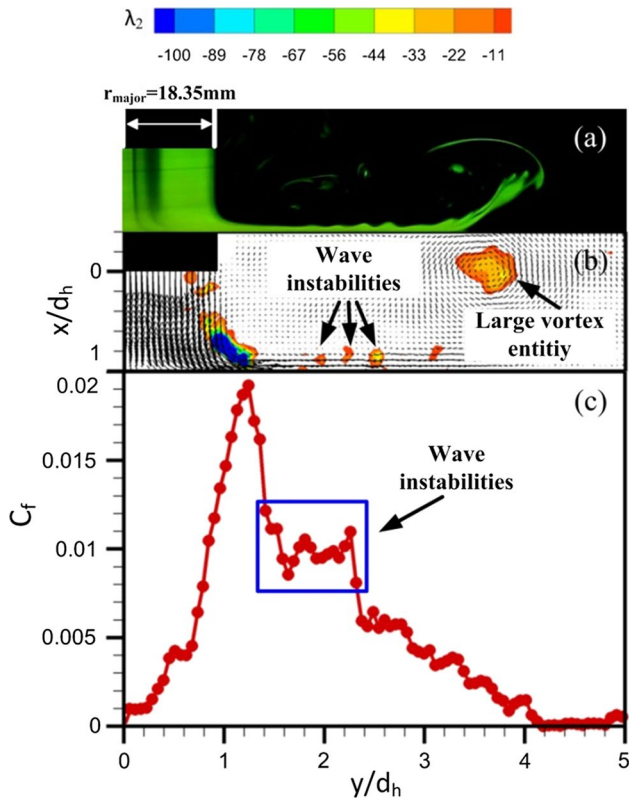
Fig. 10 Elliptic jet-flat plate impingement behaviour along major plane at $H/d_h = 1$ separation distance, as depicted through **a** LIF flow visualization snapshot, **b** instantaneous DPIV λ_2-criterion-*highlighted* region, and **c** corresponding instantaneous skin friction coefficient

strengths of the vortical structures in the $H/d_h = 1$ test case appear to be qualitatively the weakest among these three separation distances used. Similar issues appear in the λ_2-criterion-highlighted region near the impingement surface along the jet shear layer as well, due to the same reason provided for the $H/d_h = 2$ test case. The skin friction coefficient decreases once a maximum value is obtained at $y/d_h = 1.2$, before a few less-distinguishable secondary peaks appear. These secondary peaks are most likely to be produced by the wave instabilities along the impingement surface, which help maintain the skin friction coefficient at approximately $C_f = 0.01$ for a certain distance. Further downstream however, a decrease in the skin friction coefficient is observed due to the loss of flow kinetic energy and flow separations.
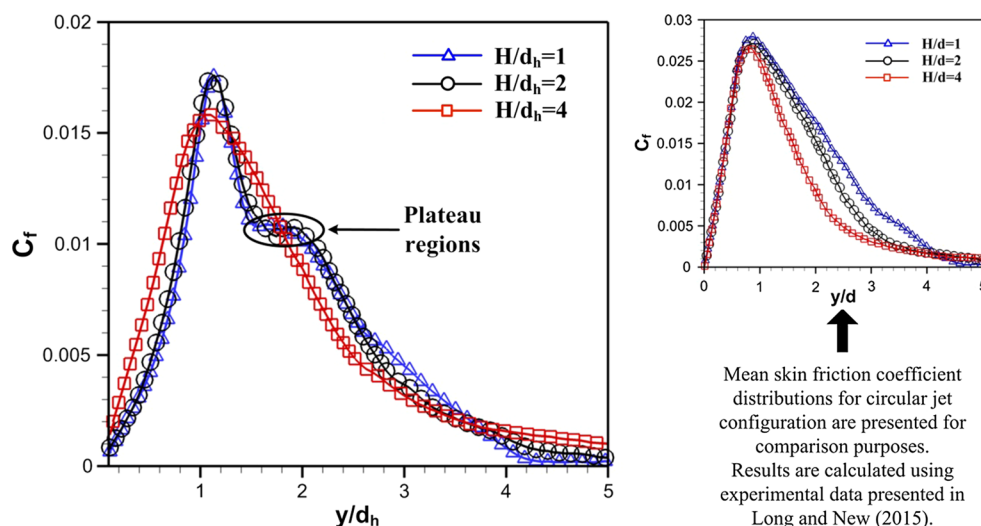
At this point, elliptic jet-flat plate impingement behaviour along its major plane appears to be grossly similar to that associated with a circular jet-flat plate impingement in terms of the jet ring-vortex and wall-separated vortex formations. However, the former still demonstrates certain unique vortical behaviour that differs from the latter. In particular, circular jet-flat plate impingements at separation distances of $H/d = 1$, 2 and 4 produce significant more coherent and independent vortex-dipoles along the flat plate without the occurrence of vortex-dipole pairings. On the other hand, the vortex-dipoles convecting along the flat plate are comparatively smaller at $H/d_h = 2$ and 4 when an elliptic jet is used instead. Interestingly, while $H/d_h = 2$ test case experiences periodic pairing of adjacent vortex-dipoles, $H/d_h = 4$ test case clearly shows the impingement of rib structures and braid vortices. Finally, wave instabilities instead of well-formed vortex-dipoles appear for $H/d_h = 1$ test case. These variations in the vortex structures and behaviour have led to interesting variations in the instantaneous skin friction coefficient distributions, and it is expected that the resulting mean skin friction coefficient distributions will reveal further differences.

Figure 11 presents the mean skin friction coefficient distributions for the present elliptic jet-flat plate impingements taken along the major plane at the three separation distances, where they can be explained by the key vortical behaviour and corresponding instantaneous skin friction coefficient distributions observed previously. For all three separation distances, the mean skin friction coefficient increases rapidly from almost zero near the impingement point to reach peak values of approximately $C_f = 0.0175$ for $H/d_h = 1$ and 2 test cases, but $C_f = 0.016$ for the $H/d_h = 4$ test case. However, before reaching the peak values, the mean skin friction coefficient for $H/d_h = 4$ test case is higher than those of the other two test cases of $H/d_h = 1$ and 2. This phenomenon can be attributed from the impingement of the braid vortices within the jet core which leads to an increase in the local skin friction coefficient for $H/d_h = 4$ test case. The peak value in the mean skin friction coefficient for $H/d_h = 4$ test case results from the impingement and subsequent turning of the jet body, as well as regular impingement of the ring-vortices and rib structures upon the flat plate.

On the other hand, those for $H/d_h = 1$ and 2 test cases are caused by the turning of the jet body and shear layer. In contrast, these values are significantly smaller than those of circular jet-flat plate impingements studied under relatively similar flow conditions by Long and New (2015). Nevertheless, the skin friction coefficient begins to decrease along the flat plate for all test cases once the peak value is attained. For that scenario, the peak value is around $C_f = 0.0275$ regardless of separation distance, as shown in the inset in Fig. 11. It should be mentioned that for that study, the circular jet nozzle diameter was $d = 20$ mm and a mean jet exit velocity of 0.11 m/s was used such that it had a mean mass flow rate that was comparable to the elliptic jets used in the present study. The jet Reynolds number in that study was approximately $Re = 2200$ and the separation distances used were $H/d = 1$, 2 and 4. Since the primary aim is to ensure that jet mass flow rates are first and foremost comparable between the circular and elliptic impinging jets here, these preceding flow conditions can be

Fig. 11 Comparisons of mean skin friction coefficients with the present elliptic jet-flat plate impingement taken along the major plane at separation distances of $H/d_h = 1$, 2 and 4, as estimated from DPIV velocity measurements. Mean skin friction coefficient distributions for circular jet-flat plate impingement at $H/d = 1$, 2 and 4 are included as *inset* in this figure

Mean skin friction coefficient distributions for circular jet configuration are presented for comparison purposes. Results are calculated using experimental data presented in Long and New (2015).

considered to be relatively close to one another and the present comparisons remain acceptable.

Returning to the present impinging elliptic jets, the skin friction coefficient for $H/d_h = 4$ test case decreases gradually before levelling off to close to zero due to wall boundary layer separations and subsequently vortex separations, similar to distributions associated with circular jet-flat plate impingements. Intriguingly, the skin friction coefficient does not decrease in such a straightforward manner for $H/d_h = 1$ and 2 test cases. For instance, these two test cases lead to initially steeper reductions in the skin friction coefficients until they incur minor plateau regions at approximately between $y/d_h = 1.7$ and 2.1. At this point, skin friction coefficient for $H/d_h = 4$ test case will be lower than those of the $H/d_h = 1$ and 2 test cases. The initially lower skin friction coefficient before the plateau regions for $H/d_h = 1$ and 2 test cases can be explained by the convections of both jet ring-vortices and rib structures after impingement for $H/d_h = 4$ test case. Moreover, the subsequent appearance of plateau regions can be explained by the initiation of closely spaced wave instabilities and jet ring-vortices at approximately $y/d_h = 1.8$ and 1.9 onwards for $H/d_h = 1$ and 2 test cases, respectively, where their presence leads to comparatively higher skin friction coefficients.

With the results associated with elliptic jet-flat plate impingements taken along the major plane presented and discussed, results taken along the minor plane will now be presented and discussed. Figures 12 and 13 show the vortex structures and vortical behaviours associated with a separation distance of $H/d_h = 4$, which are clearly different from those observed along the major plane earlier on. Similar to the earlier results, key vortical structures and behaviours are presented via instantaneous flow visualizations, DPIV velocity fields, λ_2-criterion detected regions and corresponding instantaneous skin friction coefficients,

respectively. To begin with, LIF visualizations in Fig. 12 show that the impingement behaviour along the minor plane does not indicate the presence of rib structures and braid vortices, but only jet ring-vortex impingements, wall-separated vortex initiations and vortex separations. Note that this bears close resemblance to the circular jet-flat plate impingement behaviour. Moreover, the jet ring-vortex and wall-separated vortex both possess much larger qualitative vortex core sizes along the minor plane, as compared with the major plane and circular jet configuration. From Fig. 13, key vortical locations are estimated quantitatively from the DPIV measurement results and found to be consistent with the qualitative LIF results. In this case, jet ring-vortex initiation occurs at relatively similar location as with a free elliptic jet along the minor plane at approximately $x/d_h = 1.7$ downstream of the nozzle exit.

Jet ring-vortex impingement occurs at approximately $y/d_h = 0.6$, and the wall-separated vortex separation occurs at $y/d_h = 2.4$ as shown in Fig. 13b, d, respectively. Vortex separation occurs at an even further downstream location at $y/d_h = 2.7$, as depicted in Fig. 13e. It should be noted that wall-separated vortex initiation and vortex separation locations are further away from the impingement point as compared to the previous corresponding major plane results (i.e. $y/d_h = 1.9$ and 2.4, respectively). After vortex separation, the vortex-dipole quickly loses its flow coherence through viscous diffusion instead of convecting along the flat plate, as shown in Fig. 13f. The effects of jet ring-vortex impingement, wall-separated vortex initiation and vortex separation on the instantaneous skin friction coefficient, as shown in Fig. 13, are comparatively similar to those along the major plane discussed previously. Hence, its discussion will not be repeated here for the sake of brevity.

Figure 14 shows that the flow developments for separation distances of $H/d_h = 1$ and 2 along the minor plane are
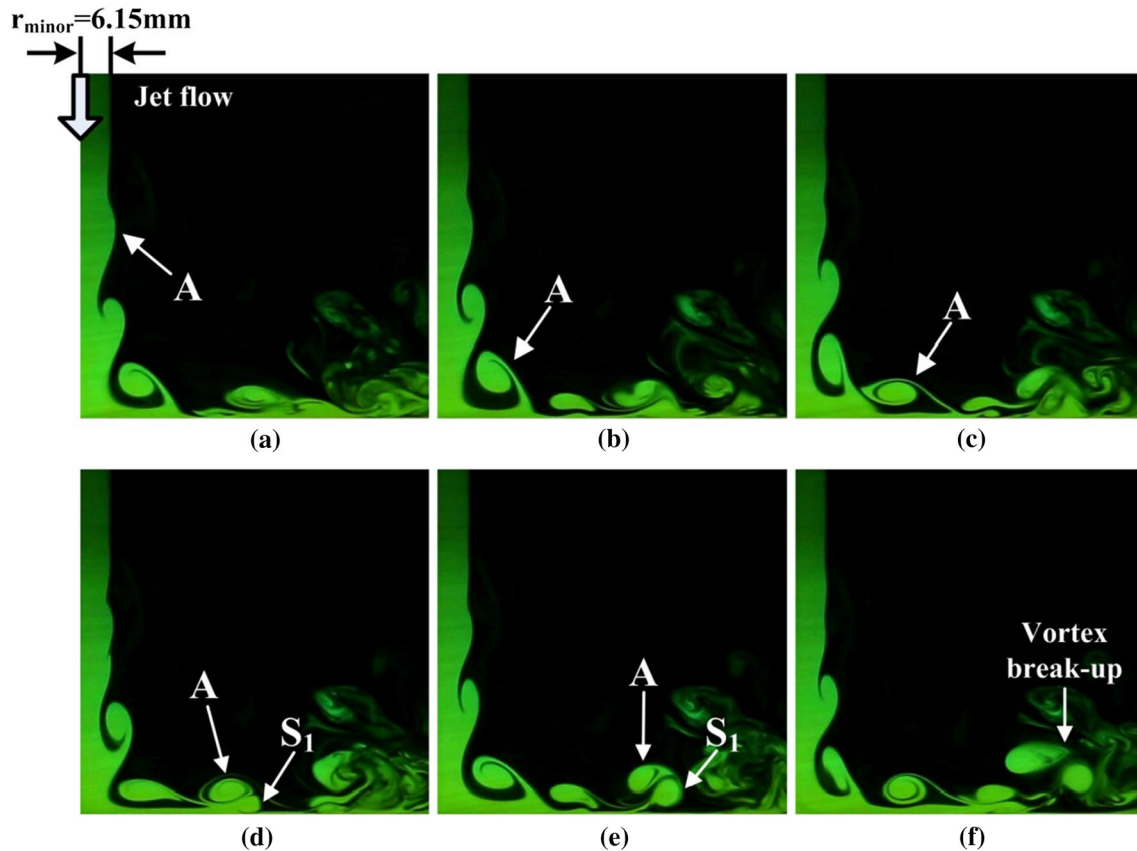
Fig. 12 Time-sequenced minor plane LIF flow images depicting the vortical behaviour associated with elliptic jet-flat plate impingement at $H/d_h = 4$ separation distance. **a** $t = 0$ s, **b** $t = 0.48$ s, **c** $t = 0.64$ s, **d** $t = 1.00$ s, **e** $t = 1.12$ s, **f** $t = 1.28$ s

remarkably similar to those of $H/d_h = 4$ test case, despite differences in the jet ring-vortex initiation location. The figure shows that jet ring-vortices are formed after the jet impinges upon the flat plate at approximately $y/d_h = 1.55$ away from the impingement point for $H/d_h = 1$ test case, while shear layer instabilities are just formed prior to jet impinging for $H/d_h = 2$ test case. Furthermore, significantly larger and better organized vortical structures are consistently produced along the minor plane as compared with those along the major plane. Recall from major plane LIF visualizations that the vortex structures tend to be less orderly and significantly smaller. Returning to Fig. 14, other than the jet ring-vortex initiation location, gross flow similarities extend to the wall-separated vortex initiation and vortex separation behaviour, both of which occur further away from the impingement point with smaller separation distances used. After vortex separation, the vortex-dipole continues to convect and pair up along the flat plate for $H/d_h = 1$ and 2 test cases, instead of transiting into incoherence rapidly seen for a larger separation distance of $H/d_h = 4$.

Since the gross vortical motion and behaviour do not vary significantly along the minor plane between $H/d_h = 1$

and 2 test cases, only the results for $H/d_h = 2$ test case will be described and discussed in detail here with the aid of Fig. 15. With reference to the figure, the wall-separated vortex is induced to form at approximately $y/d_h = 2.4$, while vortex separation occurs at approximately $y/d_h = 2.6$ shortly after. The impingement of the jet ring-vortex registers a maximum instantaneous skin friction coefficient of $C_f = 0.023$, which is higher than that of the $H/d_h = 4$ test case. Other than this peak coefficient difference, the overall subsequent flow developments of wall-separated vortex initiation and vortex separation remain quite similar to those of previous test cases.

Figure 16 presents the mean skin friction coefficient profiles associated with different separation distances along the minor plane, the distributions of which are quite different from those obtained along the major plane shown previously in Fig. 11. While the skin friction coefficients increase rapidly from almost zero to reach peak levels, they decrease gradually without appearances of any plateau regions regardless of the exact separation distance used. Comparing the peak values at different separation distances, the peak values for $H/d_h = 1$ and 2 test cases are higher than that of the $H/d_h = 4$ test case due to similar

Fig. 13 Instantaneous minor plane DPIV velocity fields and λ_2-criterion-*highlighted* regions with corresponding instantaneous skin friction coefficient associated with elliptic jet-flat plate impingement at $H/d_h = 4$ separation distance. **a** $t = 0$ s, **b** $t = 0.50$ s, **c** $t = 0.64$ s, **d** $t = 1.00$ s, **e** $t = 1.14$ s, **f** $t = 1.29$ s
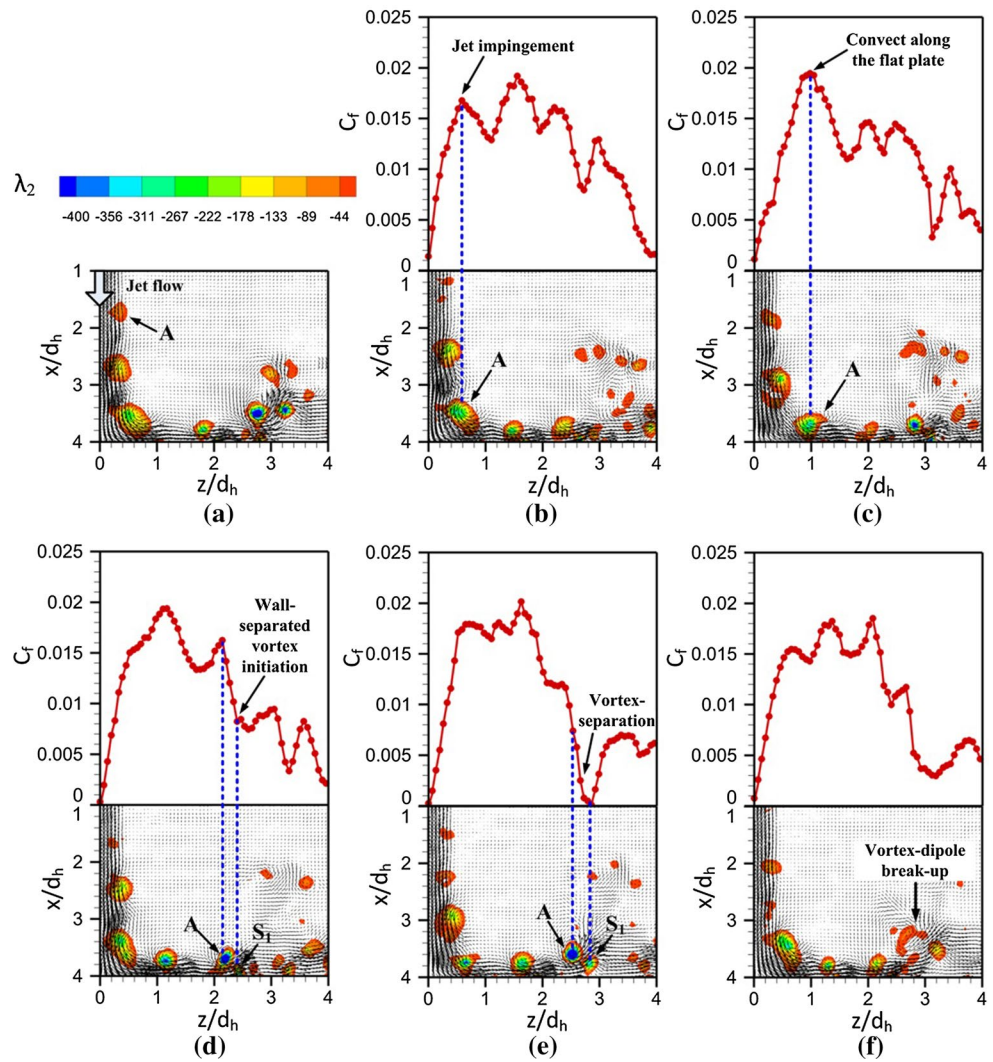

Fig. 14 LIF flow visualization snapshots depicting the vortical behaviour of elliptic jet-flat plate impingement along the minor plane at separation distances of **a** $H/d_h = 1$, **b** $H/d_h = 2$ and **c** $H/d_h = 4$
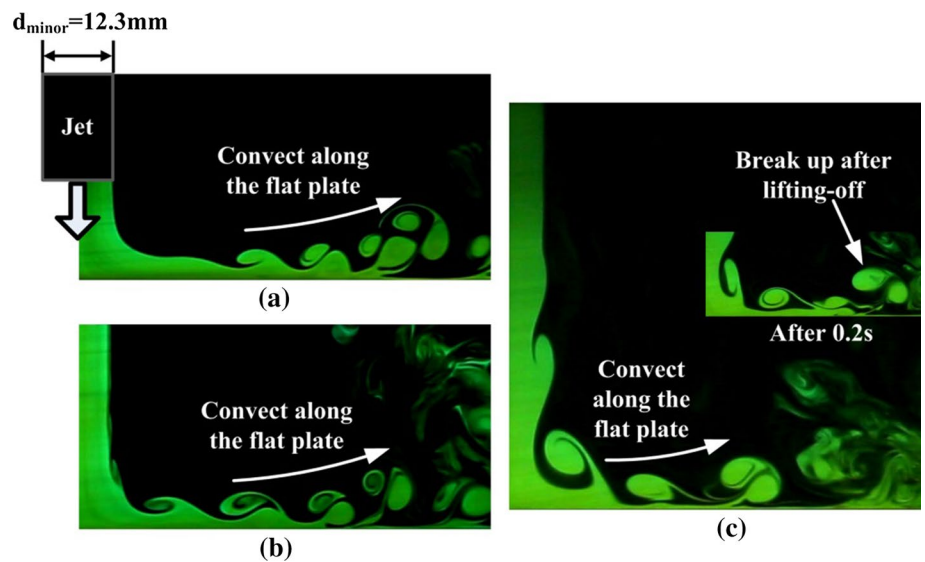
Fig. 15 Instantaneous minor plane DPIV velocity fields and λ_2-criterion-*highlighted* regions with corresponding instantaneous skin friction coefficient associated with elliptic jet-flat plate impingement at $H/d_h = 2$ separation distance. **a** $t = 0$ s, **b** $t = 0.14$ s, **c** $t = 0.36$ s, **d** $t = 0.43$ s, **e** $t = 0.64$ s, **f** $t = 0.86$ s
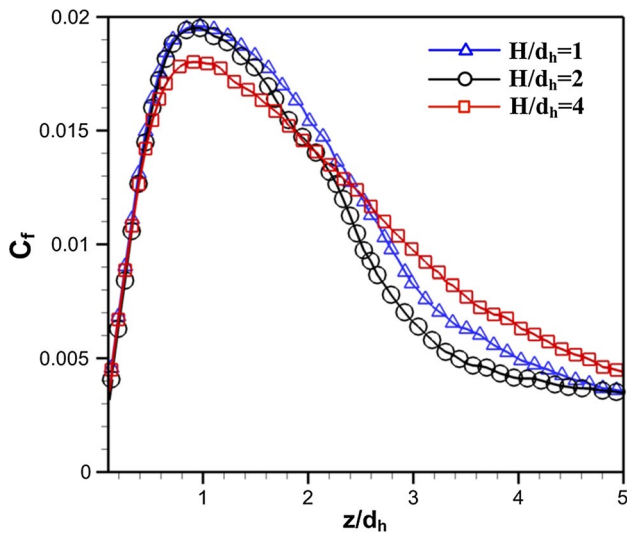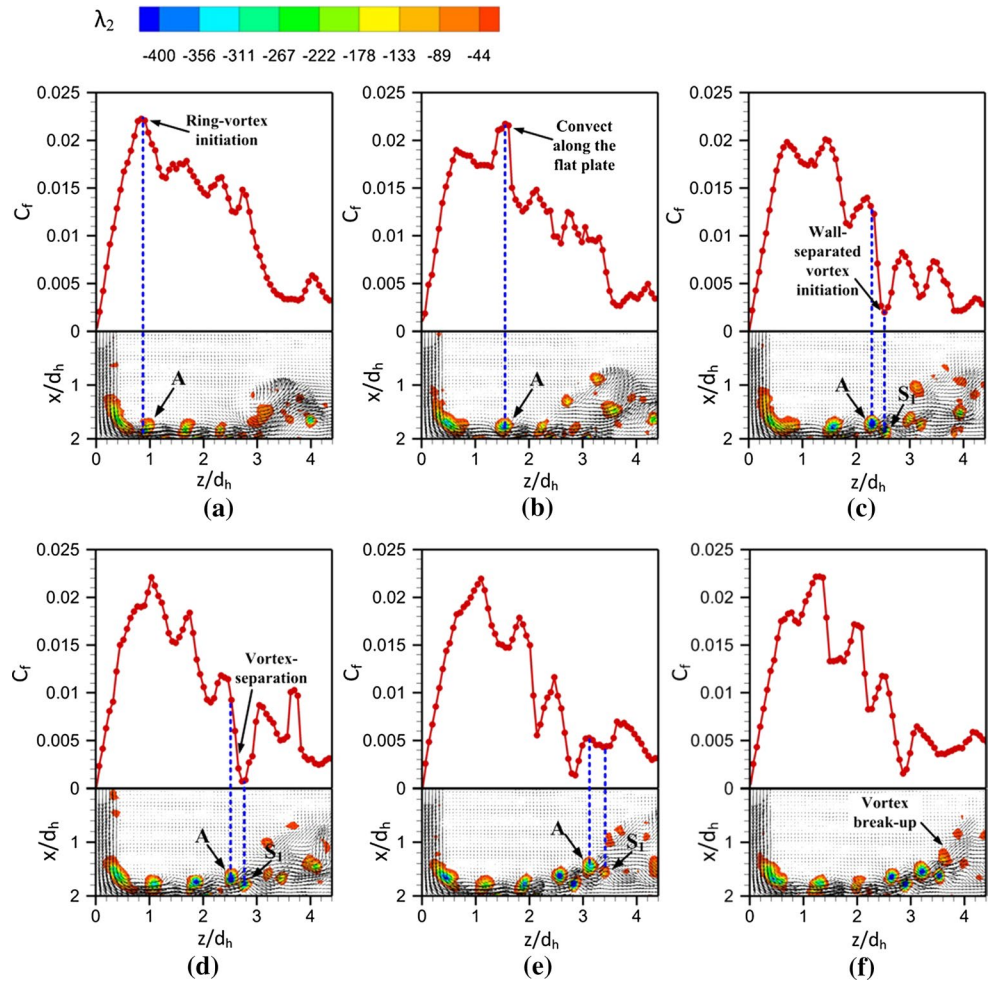

Fig. 16 Comparisons of mean skin friction coefficients associated with elliptic jet-flat plate impingement along the minor plane for separation distances of $H/d_h = 1$, 2 and 4, as estimated from DPIV velocity measurements

reasons given for observations along the major plane discussed earlier on. But interestingly, skin friction coefficient levels for the $H/d_h = 4$ test case are higher than the other two separation distances from $y/d_h = 2.4$ onwards. No plateau regions can be discerned for $H/d_h = 1$ and 2 test cases, as were seen for the same separation distance along the major plane previously. This can be explained by the fact that the distances between adjacent jet ring-vortices along the flat plate as observed along the minor plane tend to be much larger than those along the major plane, where closely spaced jet ring-vortices or wave instabilities can lead to localized distortions to the skin friction coefficient within certain locations (i.e. plateau regions). Note that the peak values along the minor plane are higher than those along the major plane, but lower than those when a circular jet is used. The mean skin friction coefficient distributions along the minor plane resemble those for circular jet-flat plate impingements, except that the former has smaller rate of skin friction coefficient reduction after the peak value has been attained.

To summarize, the vortical structures and behaviour are quite sensitive to jet-to-plate separation distance, as well as the jet plane. Results along the elliptic jet major and minor planes do demonstrate some grossly similar effects of separation distance upon the vortical structures and behaviours for the present jet impingements. For instance, for smaller separation distances, key vortical locations are located further away from the impingement point. Significant decrease in the distance between adjacent vortical structures results with reduced separation distance used, together with the physical sizes of these vortical structures. These effects, which arise from variations in the separation distance, are similar to those observed for circular jet-flat surface impingement reported by Long and New (2015). However, due to the differences in which the vortical structures evolve along the elliptic jet major and minor planes, there are some intriguing variations in the detailed flow behaviour between these two planes and circular jet impingements.

In particular, significantly more coherent vortical structures with larger vortex core sizes are produced along the minor plane. In contrast, along the major plane, $H/d_h = 1$ test case only shows a few wave instabilities while $H/d_h = 2$ and 4 test cases produce less coherent vortical structures. Moreover, the impingement behaviour of $H/d_h = 4$ test case involves more complex vortical structures on top of the jet ring-vortex and wall-separated vortex, such as the rib

structures and braid vortices. These flow differences result in distinct flow behaviours and skin friction coefficient distributions for each test case. For instance, the impingement of braid vortices and laterally inwards movement of jet ring-vortex for the $H/d_h = 4$ test case cause its skin friction coefficient level to exceed those of the other two separation distances before the peak value is reached. The later initiation of jet ring-vortex and wave instabilities along major plane for the $H/d_h = 1$ and 2 test cases, respectively, lead to the appearance of plateau regions in their mean skin friction coefficient distributions.

Lastly, the overall trajectories of jet ring-vortex and wall-separated vortex cores are tracked from their initiations to breakup, based on the imposition of λ_2-criterion upon all the DPIV velocity results. The resulting trajectories are compared to study the effects of separation distance along both major and minor planes, as shown in Fig. 17. Note that the vortex core trajectories for $H/d_h = 1$ test case along the major plane are not provided as only wave instabilities appear along the impingement surface. These vortex core trajectories were determined from the flow sequences presented before, but presented for the entire flow sequence rather than selected dataset as before.

Several interesting features can be noted from the vortex trajectories presented in Fig. 17. Firstly, as observed in the earlier LIF and DPIV results, the jet ring-vortex and wall-separated vortex initiate and subsequently combine

Fig. 17 Vortex core trajectories associated with elliptic jet-flat plate impingement along **a** major plane and **b** minor plane at different separation distances
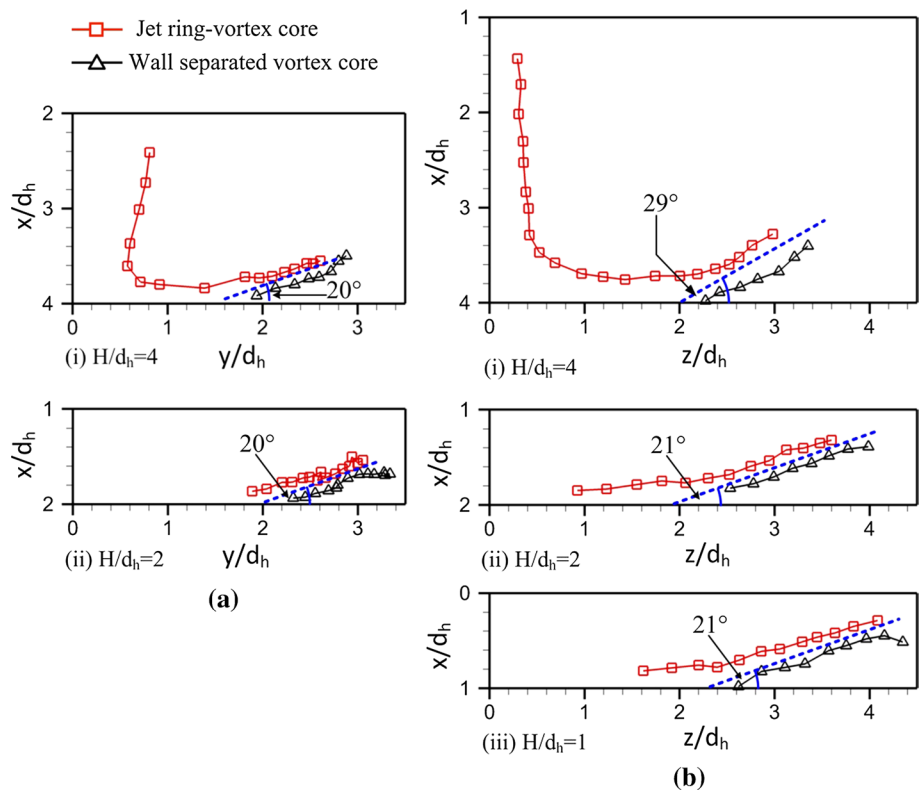
to form a vortex-dipole which lifts off from the flat plate at all separation distances along the minor plane but only for $H/d_h = 2$ and 4 test cases along the major plane. All these flow changes occur closer to the impingement point when a larger separation distance is used. It can be discerned more clearly from the vortex trajectory plots that the angle between the trajectories of the vortex-dipole after vortex separation and the flat plate is approximately 29° for $H/d_h = 4$ test case along the minor plane, which is relatively larger than the other two smaller separation distances with corresponding angles of approximately 21°. This may be attributed to a stronger vortex-dipole at the largest separation distance of $H/d_h = 4$. On the other hand, the separation angle does not vary significantly with the separation distance along the major plane. Finally, it is worthwhile to note that the distance between each vortex core along the major plane is much smaller than its counterpart along the minor plane and indicates a slower convective velocity along the former.

4 Conclusions

An investigation has been carried out on a laminar $Re_h = 2100$, AR = 3 elliptic jet impinging upon a flat plate at $H/d_h = 1$, 2 and 4 separation distances. The aim is to differentiate the effects of jet-to-plate separation distance on the vortical structures and behaviour of an impinging elliptic jet along its major and minor planes. LIF and DPIV techniques were used to provide qualitative descriptions and quantitative results of the impingement behaviour by tracking the vortical structures from their initiations to breaking-ups. Experimental results show that elliptic jet impingement behaviour is significantly more sensitive towards both the separation distance and exact jet plane than their circular jet counterparts. Nevertheless, vortex-dipole size and spacing between consecutive vortex-dipoles decrease when the separation distance is reduced. Key vortical behaviours (i.e. wall-separated vortex initiation, vortex-dipole formation and vortex separation) occur closer to the impingement point with larger separation distances. These gross influences due to separation distance variations remain relatively similar to those associated with circular jet impingements.

The general flow dynamics along the minor plane are similar and correspond well with the flow model constructed for circular jet impingements by New and Long (2015), but with larger vortex-dipoles. On the contrary, the flow dynamics along the major plane demonstrate significantly different flow features, as well as much more muted flow developments as compared to those associated with circular jet impingements. Typical flow features include impingements not only by jet ring-vortices, but also

by braid vortices and rib structures for $H/d_h = 4$ test case, vortex-dipole pairings and periodic vortical amalgamations for $H/d_h = 2$ test case, and by the appearance of a large vortex entity along the flat plate for $H/d_h = 1$ test case. These unique flow features are reflected not only in the instantaneous skin friction coefficient distributions, but in their mean distributions as well. For instance, the latter distributions show that two plateau regions occur for $H/d_h = 1$ and 2 test cases along the major plane. Additionally, skin friction coefficients for $H/d_h = 4$ test case along the major plane before the maximum value is attained are higher than those of $H/d_h = 1$ and 2 test cases, due to the impingements made by braid vortices and rib structures. Finally, vortex trajectory results are presented to further illustrate the effects of separation distance.

References

Caliskan S, Baskaya S, Calisir T (2014) Experimental and numerical investigation of geometry effects on multiple impinging air jets. Int J Heat Mass Transf 75:685–703

Coleman HW, Steele WG (1995) Engineering application of experimental uncertainty analysis. AIAA J 33(10):1888–1896

Cornaro C, Fleischer AS, Goldstein RJ (1999) Flow visualization of a round jet impinging on cylindrical surfaces. Exp Therm Fluid Sci 20:66–78

Cornaro C, Fleischer AS, Rounds M, Goldstein RJ (2001) Jet impingement cooling of a convex semi-cylindrical surface. Int J Therm Sci 40(10):890–898

EI Hassan M, Assoum HH, Sobolik V, Vétel J, Abed-Meraim K, Garon A, Sakout A (2012) Experimental investigation of the wall shear stress and the vortex dynamics in a circular impinging jet. Exp Fluids 52:1475–1489

Esirgemez E, Newby JW, Nott C, Ölçmen SM, Ötugen V (2007) Experimental study of around jet impinging on a convex cylinder. Meas Sci Technol 18:1800–1810

Fairweather M, Hargrave GK (2002) Experimental investigation of an axisymmetric, impinging turbulent jet. 1. Velocity field. Exp Fluids 33:464–471

Fleischer AS, Kramer K, Goldstein RJ (2001) Dynamics of the vortex structure of a jet impinging on a convex surface. Exp Therm Fluid Sci 24:169–175

Goldstein RJ, Sobolik KA, Seol WS (1990) Effect of entrainment on the heat transfer to a heated circular air jet impinging on a flat surface. J Heat Transf 112(3):608–611

Gutmark E, Ho CM (1986) Visualization of a forced elliptic jet. AIAA J 24:684–685

Ho CM, Gutmark E (1987) Vortex induction and mass entrainment in a small-aspect-ratio elliptic jet. J Fluid Mech 179:383–405

Husain HS, Hussain F (1991) Elliptic jets. Part 2. Dynamics of coherent structures: paring. J Fluid Mech 233:439–482

Husain HS, Hussain F (1993) Elliptic jets. Part 3. Dynamics of preferred mode coherent structures. J Fluid Mech 248:315–361

Hussain F, Husain HS (1989) Elliptic jets. Part 1: characteristics of unexcited and excited jets. J Fluid Mech 208:257–320

Jambunathan K, Lai E, Moss MA, Button L (1992) A review of heat transfer data for single circular jet impingement. Int J Heat Fluid Flow 13:106–115

Jeong J, Hussain F (1995) On the identification of a vortex. J Fluid Mech 285:69–94

Koseoglu MF, Baskaya S (2008) The effect of flow field and turbulence on heat transfer characteristics of confined circular and elliptic impinging jets. Int J Therm Sci 47:1332–1346

Landreth CC, Adrian RJ (1990) Impingement of a low Reynolds number turbulent circular jet onto a flat plate at normal incidence. Exp Fluids 9:74–84

Lee J, Lee SJ (2000) The effect of nozzle aspect ratio on stagnation region heat transfer characteristics of elliptic impinging jet. Int J Heat Mass Transf 43:555–575

Lee SJ, Lee JH, Lee DH (1994) Local heat transfer measurements from an elliptic jet impinging on a flat plate using liquid crystal. Int J Heat Mass Transf 37(6):967–976

Lim TT, New TH, Luo SC (2006) Scaling of trajectories of elliptic jets in crossflow. AIAA J 44(12):3157–3160

Lim KB, Lee CH, Sung NW, Lee SH (2007) An experimental study on the characteristics of heat transfer on the turbulent round impingement jet according to the inclined angle of convex surface using liquid crystal transient method. Exp Therm Fluid Sci 31:711–719

Long J, New TH (2015) A DPIV study on the effects of separation distance upon the vortical behaviour of jet-cylinder impingements. Exp Fluids 56:153

Longmire EK, Duong LH (1996) Bifurcating jets generated with stepped and sawtooth nozzles. Phys Fluids 8(4):978–992

Martin H (1977) Heat and mass transfer between impinging gas jets and solid surface. Adv Heat Transf 13:1–60

Moffat RJ (1988) Describing the uncertainties in experimental results. Exp Therm Fluid Sci 1:3–17

New TH, Long J (2015) Dynamic of laminar circular jet impingements upon convex cylinders. Phys Fluids 27:024109

New TH, Tay WL (2006) Effects of cross-stream radial injections on a round jet. J Turbul 7:1–20

New TH, Tsai HM (2007) Experimental investigations on indeterminate-origin V- and A-notched jets. AIAA J 45(4):828–839

New TH, Tsioli E (2011) An experimental study on the vortical structures and behaviour of jets issuing from inclined coaxial nozzles. Exp Fluids 51:917–932

New TH, Tsovolos D (2009) Influence of nozzle sharpness on the flow fields of V-notched nozzle jets. Phys Fluids 21:84–107

New TH, Tsovolos D (2011) On the vortical structures and behaviour of inclined elliptic jets. Eur J Mech B/Fluid 30:137–450

New TH, Tsovolos D (2012) On the flow characteristics of minor-plane inclined elliptic jets. Exp Therm Fluid Sci 38:94–106

Phares DJ, Smedley GT, Flagan RC (2000) The wall shear stress produced by the normal impingement of a jet on a flat surface. J Fluid Mech 418:351–375

Quinn WR (1989) On mixing in an elliptic turbulent free jet. Phys Fluids B1:1716–1722

Shi S, New TH, Liu Y (2013) Flapping dynamics of a low aspect-ratio energy-harvesting membrane immersed in a square cylinder wake. Exp Therm Fluid Sci 46:151–161

Yan WM, Mei SC (2006) Measurement of detailed heat transfer along rib-roughened surface under arrays of impinging elliptic jets. Int J Heat Mass Transf 49:159–170

Yan WM, Mei SC, Liu HC, Soong CY, Yang WJ (2004) Measurement of detailed heat transfer on a surface under arrays of impinging elliptic jets by a transient liquid crystal technique. Int J Heat Mass Transf 47:5235–5245